Unusually Strong Vertical Motions in a Caribbean Hurricane

ROBERT A. BLACK

NOAA Atlantic Oceanographic and Meteorology Laboratory, Miami, Florida

HOWARD B. BLUESTEIN

School of Meteorology, University of Oklahoma, Norman, Oklahoma

MICHAEL L. BLACK

NOAA Atlantic Oceanographic and Meteorology Laboratory, Miami, Florida

(Manuscript received 12 November 1993, in final form 31 March 1994)

ABSTRACT

Unusually strong updrafts and downdrafts in the eyewall of Hurricane Emily (1987) during its rapidly deepening phase are documented by both in situ aircraft measurements and a vertically pointing Doppler radar. Updrafts and downdrafts as strong as 24 and 19 m s^{-1}, respectively, were found. Mean updrafts and downdrafts were approximately twice as strong as those found in other hurricanes. Updrafts had approximately the same width as downdrafts. The most vigorous updrafts were located in the front quadrants of the storm, and most of the strongest downdrafts were found in the rear quadrants. The downdrafts could not be explained in terms of evaporative or melting cooling, or precipitation drag. Evidence is presented that moist symmetric instability initiated by precipitation loading may have been responsible for the strong downdrafts.

1. Introduction

Hurricanes contain maximum sustained horizontal winds that range from 33 m s^{-1} in weak storms to over 80 m s^{-1} in the most intense. Vertical velocities in the eyewall tend to be much weaker. In a study of four mature hurricanes possessing a well-developed eyewall, Jorgensen et al. (1985) (JZL) reported vertical velocities that were much weaker than the horizontal winds and mean vertical velocities that varied little with altitude. The mean of the strongest 10% of the "core" average vertical velocities was 4.2 and -2.6 m s^{-1} for updrafts and downdrafts, respectively.

Studies of tropical oceanic convection not associated with tropical cyclones, in two widely separated ocean basins, have also found weak vertical velocities similar to those in hurricanes. LeMone and Zipser (1980), using aircraft observations from an experiment in the eastern Atlantic Ocean, and Jorgensen and LeMone (1989), using aircraft observations from an experiment near Taiwan, determined that tropical oceanic convection had weak vertical velocities and they concluded that downdrafts were maintained by precipitation loading. This is in contrast to severe thunderstorms over land, in which the vertical component of the wind is often of the same order of magnitude as the horizontal component of the wind (e.g., Bluestein and Woodall 1990), and dynamic pressure forces (Rotunno and Klemp 1982; Brandes et al. 1988) may be important. Black et al. (1986b) noted that some intensifying tropical storms and weak hurricanes have "supercell" (defined as a large individual convective cell that dominates the storm's appearance on radar or in satellite images) development in which vertical velocities on the order of 20 m s^{-1} have been observed or inferred. For example, Tropical Cyclone Hilda in the South Pacific Ocean near Australia had vertical velocities, estimated in excess of 20 m s^{-1}, which were associated with a circular anvil cloud and an unusually cold cloud-top temperature (Ebert and Holland 1992).

Two research flights into Hurricane Emily on 22 September 1987 encountered unusually vigorous vertical velocities in the eyewall. Emily's track and the major aspects of the storm are found in Case and Gerrish (1988). At 1830 (all times are UTC) on 22 September 1987, Emily was centered about 220 km southeast of Santo Domingo on the island of Hispanola and was moving toward the northwest at 8 m s^{-1}. Emily had a well-defined eye approximately 25 km in diameter, and the closest convective rainband characterized by vertical velocities stronger than 3 m s^{-1} was more than 70 km from the outermost eyewall echo (cf. Fig.

Corresponding author address: Robert A. Black, NOAA/ERL/HRD/AOML, 4301/Rickenbacker Causeway, Miami, FL 33149.

1). At all times during these flights, part of the storm's outer circulation was over Hispanola. Emily was an example of a "rapidly deepening" storm according to the criteria for typhoons established by Holliday and Thompson (1979). In the 24-h period beginning at 1800 21 September, Emily's central pressure dropped at an average rate of 1.8 mb h^{-1}. The strongest radar reflectivity occurred in the front quadrants, as did most of the strong updrafts. Strong updrafts and downdrafts were encountered at all flight levels, that is, 3, 4, 5, and 5.5 km (all heights are MSL).

The purpose of this paper is to document the occurrence of unusually strong updrafts and downdrafts in a hurricane using both in situ data and vertically pointing Doppler radar measurements, and to offer a plausible explanation for these findings. In section 2, we discuss the data and data-analysis techniques. The results of our analyses are given in section 3. Section 4 contains a summary and conclusions.

2. Data and data analysis

All of the data were collected aboard the two NOAA WP-3D aircraft operated by the Aircraft Operations Center (AOC). Only one aircraft (NOAA-43, I) was equipped with a Doppler processor for its 3.2-cm radar in the tail. The tail radar scanned in the plane perpendicular to the aircraft track; for this flight, upward- or downward-pointing Doppler radials were recorded every 3 s. With a typical aircraft ground speed of approximately 135 m s^{-1} and the 10 rpm antenna rotation rate, the horizontal resolution of the Doppler data is about 0.8 km. Although this aircraft flew most of its penetrations at about 3 km, a few of its penetrations were at 4.5 and 5.0 km. The other aircraft (NOAA-42, H) flew at several altitudes from about 4.8 to 5.5 km. Except for the Doppler radar on I and a pair of vertically pointing electric field mills on H, both aircraft carried identical instruments that were described by Jorgensen (1984a).

As in most other hurricane studies, the pilots did not maneuver to encounter or avoid strong reflectivity regions in the eyewall. Instead, the flight patterns were arranged in advance. The I aircraft flew radial legs about 80 km in length, and successive radial legs were separated in the downwind direction by about 60°. The H aircraft flew pie-shaped paths of various radial lengths that also rotated about the center of the storm. This aircraft's downwind legs were flown at several radii outside the eyewall between 30 and about 100 km.

The draft data are considered both on a quadrant by quadrant basis and for the storm as a whole. The radial penetrations of the eyewall that are considered in this study were well distributed around the storm (Fig. 1). Figure 1 also shows the asymmetric radar reflectivity structure of the eyewall. The area with echo stronger than 40 dBZ in the eyewall greatly increased from Figs. 1a and 1b.

a. In situ vertical velocity measurements

The vertical component of the wind on both aircraft was computed with an algorithm developed by AOC (J. Leise, personal communication). This algorithm identifies and removes spikes from the data, filters the time derivative of the radar altimeter time series with a low-pass filter, and the vertical accelerometer time series with a high-pass filter. Filtering was done in two stages: first, the raw 1-s data were filtered forward, then backward in time, using a first-order autoregression filter on the previous five values. The filtered output from the forward pass was added to that from the backward pass and averaged, thereby removing any offsets introduced by the filter. The sum of these two quantities is the vertical ground speed (WGS). The vertical speed of the air with respect to the aircraft (WAS) is computed in the standard way using the "gust equation" (Axford 1968; JZL; Jorgensen and LeMone 1989) and has an absolute accuracy of about ± 1 m s^{-1}. Vertical velocity is obtained by subtracting WGS from WAS. These values are computed with a resolution of 1 Hz. Direct comparisons of Leise's algorithm with the JZL method showed that the average algebraic difference (JZL − Leise) was -0.4 m s^{-1} (0.8 m s^{-1} rms) with a peak difference of -3 m s^{-1}. These differences were attributed to the use of a different high-pass filter (JZL used a 30-s period Graham filter) and were considered to be negligible because they are within or near the 1 m s^{-1} accuracy limits of the P-3 winds (J. Leise, personal communication). We chose the AOC algorithm because of its superior performance when data gaps occurred.

For comparison purposes, the Emily vertical velocity events were computed using the "core" definition of JZL. A core was defined from the vertical velocity w time series as an event in which w was of the same sign and had a magnitude of at least 1 m s^{-1} for at least 4 s, which corresponds to a distance of at least 0.5 km. As in JZL, it was not possible to relate individual cores to either the stage in the lifetime of the convection or to a particular convective cell. The average vertical velocity $\bar{w}$ was computed for each core. We focused most of our attention on the cores with the highest 10% of the averaged vertical velocities, which included all of the (extreme) 1-s events of at least 15 m s^{-1}.

Updrafts and downdrafts were considered separately. Distance from the storm center, quadrant, altitude, width, average temperature, and average total water contents were computed for each core. Many of these parameters are correlated with each other in that the widest cores also tended to have the greatest mean velocity and the highest peak 1-s velocity.

All of the extreme vertical velocity events occurred in the eyewall. In this case, the location of the eyewall based upon the radar reflectivity data was about 17.5 km from the center. The radius of the maximum horizontal wind speed (RMW) was typically 10–15 km

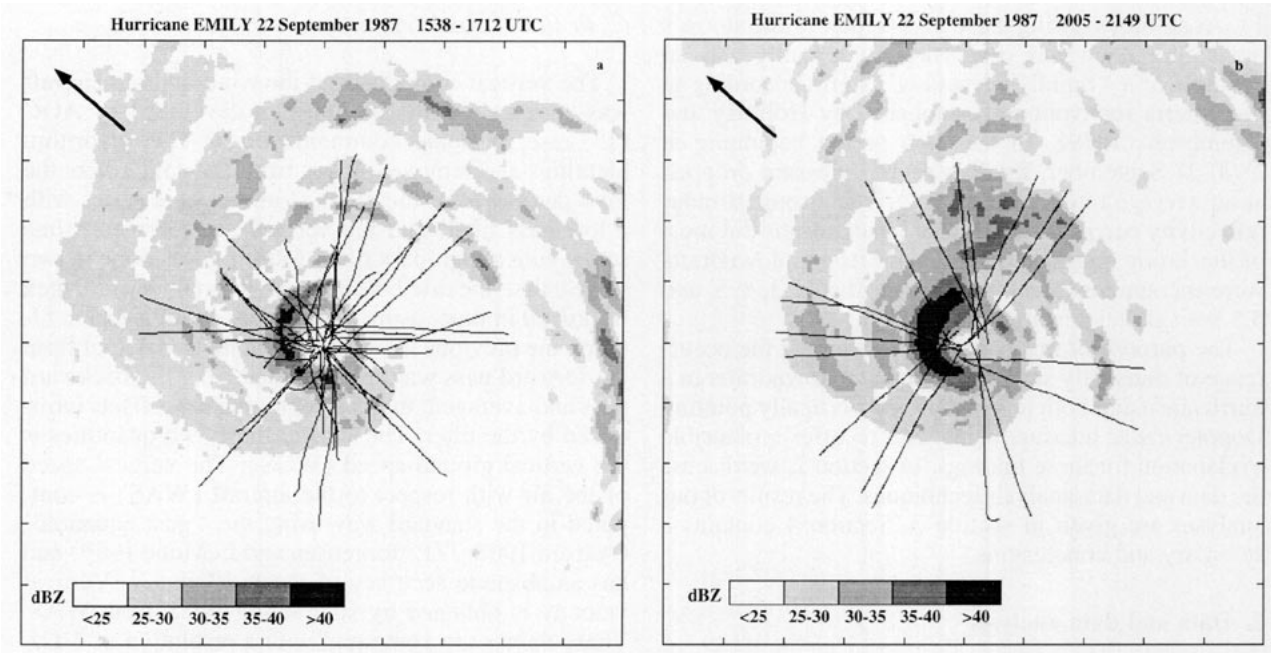

FIG. 1. (a) Hurricane Emily composite radar reflectivity factor at flight level of I from 1538 to 1712 UTC. Positions of the radial legs from upper aircraft are indicated by lines. The domain is 240 km on a side. Tick marks are 24 km apart. The heavy arrow shows the direction of the storm motion. (b) Same as (a) but the composite is from 2005 to 2149 UTC. The radial legs flown by the Doppler aircraft are shown. Note the increase in the area of the 40 dBZ or greater reflectivity in the eyewall for this composite.

from the wind center. The RMW was determined from the horizontal wind measurements taken along the radial legs by filtering the 1-s values with an 11-point binomial filter, and then locating the aircraft position at the time of the highest filtered wind speed. The cores were ordered by quadrant as well as vertical velocity. The draft data were considered separately for each aircraft and also by combining the data from both aircraft. No significant differences in either the size or strength of the cores were observed by each aircraft. However, since H made more than twice as many eyewall penetrations as I, it is possible that the extreme values observed by I may have been even greater had that aircraft flown more penetrations.

JZL discuss the effect of the shape of the vertical core on the observed core magnitude and the effects of not penetrating the center of the core. They show that if the core vertical velocity profile as a function of time resembles a triangle, and if the aircraft fails to penetrate the exact center of the core, the true maximum vertical velocities could be up to twice as strong as those observed by the aircraft. However, we believe that since these cores were unusually broad and smooth, it is unlikely that the peak vertical velocities for these extreme events were much higher than those we observed.

b. *Vertically pointing Doppler measurements*

Vertically pointing Doppler radar data were also collected from I for each of the 18 eyewall penetrations made by that aircraft. These data were unfolded manually in a manner similar to that used to unfold the horizontal wind data. Vertical velocity w is related to the mean particle fall speed V_t, the vertical speed of the Doppler radar antenna on the tail of the aircraft V_a, and the Doppler velocity V_r as follows:

$$w = V_r - V_t + V_a. \quad (1)$$

The mean particle fall speed is a function of particle phase, bulk density (in the case of ice particles), diameter, and air density. The following relations between radar reflectivity factor Z and fall speed for ice particles (above 7.1 km) and raindrops (under 5.1 km) were given by Marks and Houze (1987):

$$V_t = \begin{cases} 2.6Z^{0.107}, & \text{for altitudes} < 5.1 \text{ km} \quad (2a) \\ 0.817Z^{0.063}, & \text{for altitudes} > 7.1 \text{ km}. \quad (2b) \end{cases}$$

However, no density correction was applied to the ice particle fall speeds. As in Marks and Houze (1987), in the transition layer between regions containing mostly ice particles and regions with rain, the V_t was interpolated linearly from a water V_t at the bottom to an ice particle V_t at the top.

In the stratiform precipitation areas, the melting layer is characterized by a rapid increase in particle fall speed (and V_r) as ice particles melt in the layer. Since the melting layer is often accompanied by a relative maximum in the reflectivity, the brightband level is defined as the middle of the melting layer. The brightband level

was easily found by examining the change with height of $V_r(\Delta W)$ over a shallow depth, usually at 5 km $\pm$ 1 km. If the peak ΔW is at least 1.5 m s^{-1} per gate (one gate is 300 m in this case), the brightband level is defined as the level at which ΔW is a maximum; otherwise, the brightband is defined as the center of the original layer. The top and bottom of the melting layer are set to plus/minus one gate, respectively, above and below the brightband level.

In the eyewall, a more complex procedure was necessary. In convective areas the transition zone between areas with mostly ice particles and those with predominantly liquid drops is much more difficult to define than the melting layer is in stratiform areas because vigorous vertical motions often advect substantial quantities of liquid water high above the height of the 0°C isotherm. There is no sharp gradient of either V_t or V_r in such places, and supercooled raindrops and wet-surfaced graupel often coexist. In this case, the change in the supercooled water content with altitude becomes an important consideration. Since the eyewall in Hurricane Emily was also more vertically oriented (Fig. 2; see the right side of the figure) than those shown by Jorgensen (1984b) and Black (1993), large particles could have been carried far above the melting level.

To reduce underestimates of V_t in the eyewall, the magnitudes of both V_r and reflectivity from 5- to 12-km altitude were used to recalculate the height and depth of the transition layer. As before, the bottom of the transition layer was set equal to the level of the bottom of the stratiform area melting layer. The new top of the convective transition level was defined as the first level below 12 km (or the top of the reflectivity data, whichever was lower) at which the reflectivity was greater than 20 dBZ and the V_r was at least 2 m s^{-1} or less than -4 m s^{-1}. If the depth of the transition layer exceeded 2 km, the bottom of the transition layer was raised to the level that was one-quarter the distance between the previous bottom and top of the transition layer. A new "convective" brightband level was defined as the midpoint of the new transition layer. This procedure was repeated until the depth of the transition layer was less than 2 km.

These thresholds were determined subjectively based upon a visual inspection of the estimated values of V_t and w, the vertical velocity as a function of altitude for a large number of radial penetrations of the eyewalls of several hurricanes. The estimated values of V_t are not very sensitive to small ($\pm$10%) changes in the transition-layer criteria.

c. *Microphysical data*

Microphysical data collected by the aircraft included 2D particle image data in the cloud particle range of 0.05–1.6 mm (2D-C) and the precipitation particle range of 0.2–6.4 mm (2D-P). These data were used to estimate qualitatively the water loading of the drafts.

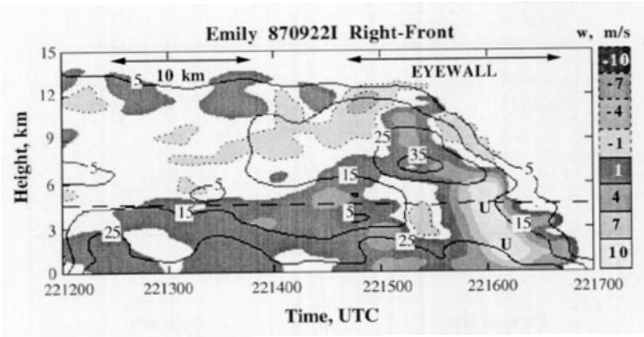

FIG. 2. A representative radar reflectivity (solid contours in dBZ) and Doppler-derived vertical velocity (m s^{-1}; lowest value for gray scale at right) cross section through the right-front quadrant. The altitude of the Doppler aircraft is indicated by the dashed line. In this and all other Doppler cross sections a "U" highlights the location of Doppler-derived updrafts greater than 15 m s^{-1}, and a "D" marks the location of Doppler-derived downdraft speeds in excess of 15 m s^{-1}.

The image data were analyzed following the methods described by Black and Hallett (1986) and Houze et al. (1992). All of the 2D data from the H aircraft were averaged for 6 s (corresponding to the tail radar antenna rotation period), which gives a horizontal resolution of about 0.9 km. To compute water contents from 2D images of ice particles, it is necessary to determine the effective bulk density of the ice particles. We used the method described by Black (1990) to obtain the effective ice particle bulk density at a 6-s time resolution. Particle image data from the I aircraft were averaged for 10 s, which corresponds to a horizontal resolution of about 1.4 km. The longer averaging time was used in this case to obtain a more stable estimate of the raindrop size distribution for calibrating the radar. Since these data were acquired in rain, no special processing was necessary to compute water contents. Cloud droplet liquid water content was obtained with the Johnson–Williams (JW) liquid water content meter. This device uses a heated platinum wire for a sensor and is sensitive principally to drops less than about 0.03 mm in diameter (Knollenberg 1972).

3. Results

The cumulative distribution sorted by mean core vertical velocity is presented in Fig. 3. The 50% and 90% levels of the distribution are emphasized. JZL's comparable values for the strongest cores (marked on Fig. 3) were 4.2 and -2.6 m s^{-1} for updrafts and downdrafts, respectively. While the 90% value of the mean updraft core vertical velocity was slightly stronger, the 90% level of the distribution for Emily's downdrafts was almost twice as strong as that given by JZL.

a. *Flight-level updrafts*

Table 1 lists average values and the range of the core vertical velocity by quadrant in order to determine their

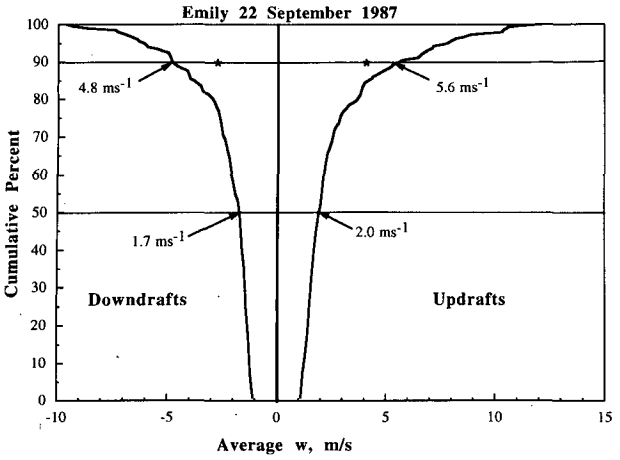

FIG. 3. Cumulative distribution of the mean vertical velocity for all cores. The asterisk on the 90% line represents the corresponding values for updrafts and downdrafts from JZL.

spatial distribution. The strongest mean updrafts were observed on the inside edge of the eyewall in the left-front quadrant, and in the right-front quadrant. Table 1 shows that although the front quadrants contained the majority of the strongest updrafts, no quadrant was devoid of strong updrafts. Furthermore, the magnitudes of the mean cores did not differ significantly (according to the *t* test) among quadrants. Asymmetries in the core distribution are evident in Table 1. The front quadrants contained twice as many updraft cores as downdrafts, whereas in the rear quadrants, the numbers of up and downdraft cores were about equal. The right-front quadrant contained mostly large updrafts, and the left-rear quadrant had twice as many downdrafts as updrafts. The right-rear quadrant contained more updrafts than downdrafts, but the downdrafts were stronger; the left-front quadrant had about equal numbers of up and downdraft cores.

The distribution of peak 1-s vertical velocities followed that of the mean updrafts. The record flight-level updraft (23.9 m s^{-1}) was observed in the right-front quadrant at 5 km; the second strongest updraft at 5 km (20.7 m s^{-1}) was in the same quadrant. At 3 km, the strongest 1-s updraft (23.5 m s^{-1}) was in the left-front quadrant; the second strongest (20.6 m s^{-1}) was in the left-rear quadrant. In view of the ± 1 m s^{-1} accuracy of the vertical velocities, there is no significant difference in the peak 1-s updraft velocities observed at 3 and 5 km. Even though there were approximately twice as many measurements made near 5 km, there were still enough measurements made at 3 km to be statistically significant.

Draft widths were not correlated with vertical velocity. The widest updrafts by quadrant (mean width 7.5 km) occurred in the right-rear quadrant, and the narrowest (mean width 2.5 km) were found in the left-rear quadrant. The second strongest and second widest updrafts occurred in the right-front quadrant. The difference in the mean core widths on the right and left sides of the storm is significant at the 95% level according to Student's t-test, suggesting that the widest updrafts were found on the right side of the storm track and the narrowest updrafts were on the left side. Overall, Emily's drafts were about three times as wide as the GATE [GARP (Global Atmospheric Research Program) Atlantic Tropical Experiment] drafts presented by JZL, but were only slightly wider than the eyewall drafts of JZL.

The average of the mean updrafts in this sample (Table 1) were twice as strong as the mean top 10% level updrafts observed in the tropical eastern Atlantic Ocean (LeMone and Zipser 1980). They were also stronger than the updrafts observed in oceanic cumuli east of Taiwan (Jorgensen and LeMone 1989). The updrafts observed in the eyewall of Emily were similar in size and magnitude to the updrafts observed in various tropical cyclone "supercell" cases (Ebert and Holland 1992). However, unlike the storms containing a "supercell," Emily had an eyewall that contained strong updrafts in *all* quadrants of the storm for a relatively long period of time (at least 7 h).

b. Downdrafts

Downdrafts were arranged in the same manner as the updrafts; however, the most extreme cases did not usually occur in the same quadrants as the updraft extrema. More of the strong downdrafts occurred on the left side of the storm than on the right side. The strongest mean

TABLE 1. Emily eyewall 10% level vertical core data summary at flight level. Drafts are sorted by quadrant. Comparisons with GATE and the hurricane vertical velocities reported by Jorgensen et al. (1985) are listed under JZL. For the strongest 10% of all cores sorted by quadrant, $\bar{w}$ is the mean of the average core magnitudes, $\overline{w_{max}}$ is the mean of the peak 1-s vertical velocities in each core, and N is the number of each type of core (up or down) encountered. Values for updrafts and downdrafts are on separate lines. Data for downdrafts are in parentheses.

Quadrant	$\bar{w}$ (m s^{-1})	$\bar{w}$ range (m s^{-1})	$\overline{w_{max}}$ (m s^{-1})	w_{max} range (m s^{-1})	Width (km)	N
Right front	8.5	6.5–11.2	17.0	13.0–23.9	6.5	9
	(5.0)	—	(12.5)	—	(5.6)	1
Left front	8.3	5.7–12.1	14.9	7.2–23.5	4.5	11
	(5.4)	(4.7–6.1)	(8.9)	(6.9–11.8)	(4.5)	8
Right rear	7.0	5.6–8.1	12.3	8.7–14.6	7.5	7
	(6.9)	(4.9–8.6)	(13.1)	(9.8–18.6)	(6.4)	4
Left rear	7.9	5.6–10.5	14.6	10.3–20.6	2.5	5
	(6.9)	(4.8–9.6)	(12.7)	(7.1–18.8)	(4.4)	9
All data	8.0	5.6–12.1	14.9	7.2–23.9	5.4	32
	(6.3)	(4.7–9.6)	(11.4)	(6.9–18.8)	(4.6)	22
JZL						
Eyewall	4.2		8.2		4.4	
	(2.6)		(5.0)		(3.0)	
GATE	4.2		7.2		1.8	
	(2.6)		(4.5)		(1.4)	

downdraft in Emily (9.6 m s^{-1}) was observed in the left-rear quadrant (Table 1), the same quadrant that contained the narrowest updrafts. Similarly, the only right-front quadrant downdraft was one of the weakest downdrafts of the upper 10% sample. Half the mean downdraft speeds were in excess of 1.7 m s^{-1}. Within the cores, the peak 1-s vertical velocity occurred in the quadrant with the strongest average core magnitude. The strongest downdraft at 5 km (18.8 m s^{-1}) was in the left-rear quadrant; at 3 km, it (18.6 m s^{-1}) was in the right-rear quadrant (Table 2). These values are more than twice as strong as those obtained in the front quadrants. Overall, the downdraft magnitudes were about twice as strong as those in the eastern Atlantic (LeMone and Zipser 1980), other hurricane eyewalls (JZL), and near Taiwan (Jorgensen and LeMone 1989).

The peak water contents observed in each downdraft as computed from the 2D-P and 2D-C probe data are presented in Table 2, along with vertical wind, width, and average-altitude data. Since the size ranges of these probes overlap, and the 2D-C has better resolution than the 2D-P, we assume that the larger of the two probe data values best represents the water content at the time of observation. If there are many small particles, the 2D-C data are more accurate, while if there are many large particles, the 2D-P data are probably more accurate. These data show that at 3 km there was up to 16 times more precipitation than at 5 km and higher passes. All but one of the passes with peak water content in excess of 7.5 g kg^{-1} were observed below 3.1-km altitude.

c. *Vertically pointing Doppler winds*

The vertically pointing Doppler wind measurements presented in this section provide independent evidence of the strong updrafts and downdrafts measured by the in situ sensors aboard the aircraft. The appearance of the right-front quadrant vertical motions as revealed by Doppler radar is shown in Fig. 2. The vertically continuous eyewall updraft channel from the surface to about 12 km was a persistent feature in the right-front quadrant. This quadrant contained only one of the strongest downdrafts (Table 2), and it was one of the weakest of those.

Figure 4 shows an example of cross sections of Doppler vertical velocity and reflectivity fields along with flight-level (3 km) data in the left-front quadrant. The most striking feature of this quadrant (Fig. 4a) is the strong eyewall Doppler updraft at the time of maximum wind (Figs. 4b,d), flanked on both sides by deep,

TABLE 2. The strongest 10% downdrafts in the storm ranked by average vertical velocity $\bar{w}$. Here ID refers to the aircraft that obtained the measurement, I is NOAA-43, and H is NOAA-42. The speeds $\bar{w}$ and w_{max} are in meters per second, width is in kilometers, and 2D-P and 2D-C water contents are in grams per kilogram (values in excess of 7 g kg^{-1} are highlighted in boldface type). Start and stop times for the cores are UTC. Altitude is in meters.

Rank	ID	Start	Stop	$\bar{w}$	w_{max}	Width	Altitude	2D-P	2D-C
Right front									
17	I	2217:42	2218:15	−5.0	−12.5	2.9	4582	0.3	0.14
Right rear									
3	I	2107:52	2109:12	−8.6	−18.6	10.6	2659	4.0	2.1
4	H	1812:06	1812:54	−7.4	−11.6	6.9	4708	0.6	2.6
7	H	1605:02	1605:41	−6.8	−9.8	4.9	4810	0.6	1.1
19	I	2109:14	2109:36	−4.9	−12.5	3.0	2592	0.6	
Left rear									
1	H	1746:38	1746:52	−9.6	−14.1	2.0	4806	0.7	2.1
2	H	2118:45	2119:24	−9.3	−18.8	5.6	4975	2.1	2.9
5	H	2101:58	2102:26	−7.3	−15.4	5.0	5272	1.0	
6	I	2104:18	2104:53	−7.0	−12.7	5.3	2812	**17.5**	**13.3**
8	H	1730:52	1731:20	−6.8	−13.5	4.1	4727	0.7	1.4
9	I	1623:57	1624:10	−6.4	−12.2	2.1	3073	**17.3**	**15.9**
10	H	2152:01	2152:35	−6.3	−12.8	5.9	5775	1.4	1.7
16	I	1657:56	1658:29	−5.0	−7.1	4.9	2925	**16.9**	**11.6**
21	I	2104:01	2104:10	−4.8	−7.7	1.5	3003	**7.8**	**13.0**
Left front									
11	H	2035:30	2035:56	−6.1	−11.8	4.3	5608	3.3	3.4
12	H	2019:34	2020:19	−6.0	−9.1	6.0	5482	1.1	**8.3**
13	I	1830:41	1831:08	−5.9	−9.9	3.0	2954	**7.5**	**8.3**
14	H	2105:24	2105:56	−5.5	−8.2	5.1	5245	2.9	
15	H	1903:21	1903:38	−5.3	−8.9	2.6	5159	3.4	4.3
18	H	1734:04	1734:17	−4.9	−6.9	2.1	4824	0.7	1.4
20	H	2039:55	2040:44	−4.9	−9.3	8.3	5559	4.3	2.3
22	H	2039:15	2039:23	−4.7	−7.0	1.5	5474	1.1	1.4

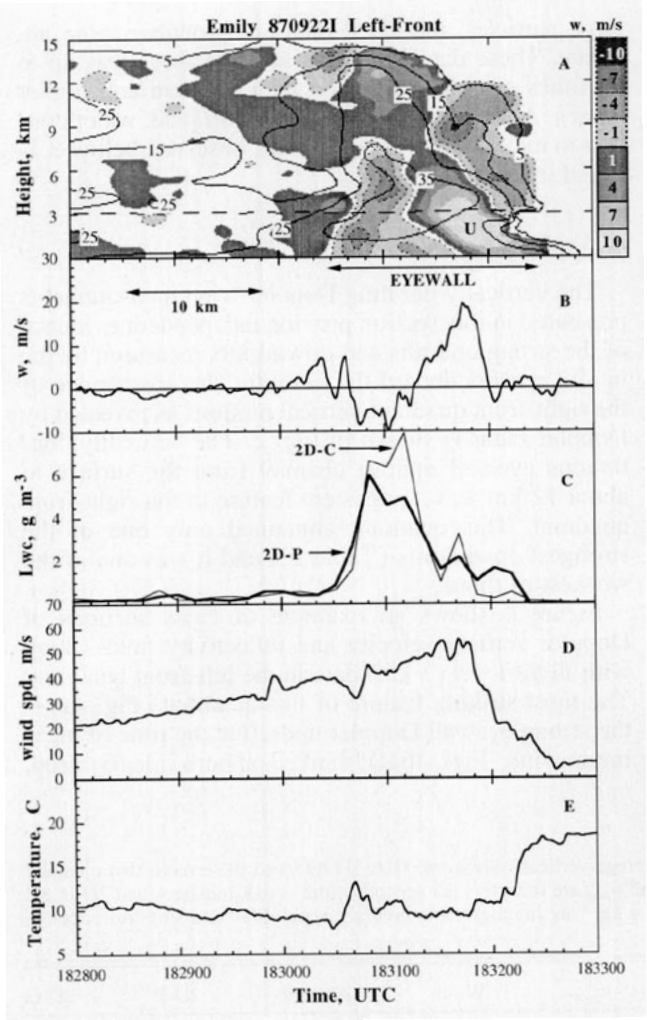

FIG. 4. Vertical cross section of (a) Doppler-derived vertical velocity and reflectivity (a as in Fig. 2), (b) plus flight-level vertical velocity, (c) precipitation water content, (d) horizontal wind speed, and (e) temperature for Doppler pass 9 in the left-front quadrant. The position of the Doppler aircraft is shown in (a) as the dashed line at approximately 3-km altitude.

strong downdrafts. The radially outward sloping downdraft contained moderate precipitation (Fig. 4c), whereas the inner downdraft (which was mostly above flight level) was barely represented in the flight-level vertical winds (Fig. 4b). The Doppler-derived vertical winds and the flight-level vertical winds match up well. A temperature increase (Fig. 4e) consistent with compressional warming marked the aircraft's entry into the broad outer downdraft. Downdraft zones that are wider near the surface (as in Fig. 4a) are not common in the hurricane eyewall. This may indicate that the downdraft air is diverging at the surface. The horizontal wind speed (Fig. 4d, at 1830:40) in the downdraft decreased slightly at the same time that a small relative maximum in temperature (Fig. 4e) occurred. We believe this decrease in wind speed was a result of vertical mixing with air having lower horizontal momentum above flight level. The outward slope of the reflectivity contours between the surface and 15 km in this portion of the eyewall is about 35° from the vertical, which is in accord with other observations (Jorgensen 1984b; Marks et al. 1992).

Another example of a strong downdraft in the left-front quadrant is shown for a radial pass in approximately the same portion of the eyewall as in Fig. 4 but for 2 h later (Fig. 5). This time the downdraft at 2032:30 was 9 km deep and had a maximum flight-level speed of approximately -8 m s^{-1}. The Doppler-derived vertical velocity field indicated that the strongest part of this downdraft was near 5 km. The 3-km flight-level data (Figs. 5b–e) showed that the highest precipitation liquid water content on both probes occurred near the RMW in the strong updraft, not in the downdraft as in Fig. 4. This updraft had the strongest vertical velocity observed at this level. A temperature

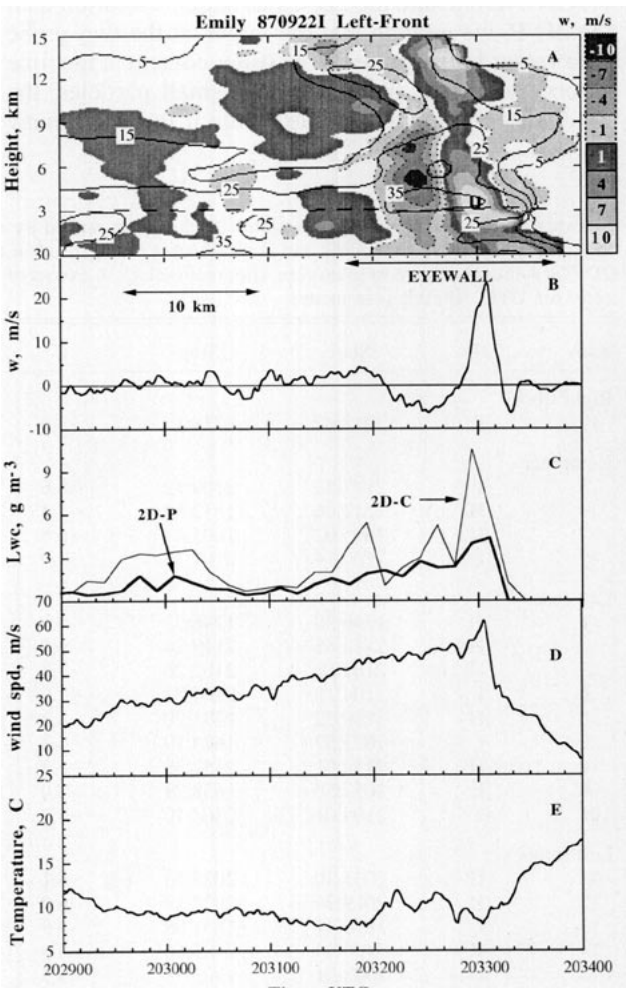

FIG. 5. As in Fig. 4 but for Doppler pass 13 in the left-front quadrant.

rise in the broad downdraft at 2032:10, consistent with compressional warming (Fig. 5e), was also present on this pass. If a saturated parcel at the temperature and pressure of the H flight level is lifted along the appropriate moist adiabat until it reaches the altitude of the top of this downdraft, it would have a temperature of about −22°C. Since the H aircraft flight level is above or near the melting level, the entire air column above about 5 km is cooler than 0°C and therefore melting could not have contributed to the initiation of this downdraft. Once again, there was also a downdraft on the inside edge of the eyewall updraft; however, this time it was strongest at flight level.

The rear quadrants of the eyewall were dominated by broad downdrafts that contained substantial amounts of precipitation. A radial leg that penetrated the left-rear quadrant of the eyewall (Fig. 6) encountered a downdraft zone at approximately 2104 that extended from the surface to at least 12 km. At flight level, this wide downdraft occurred at the RMW (Figs. 6b,d), where the updraft is observed in other quadrants, and contained substantial precipitation (Fig. 6c). The core of this downdraft (Fig. 6e) was cooler than its surroundings. On this pass, the patchiness of the updrafts above 5 km at 2105 is in sharp contrast to the vertical continuity of the downdrafts.

A broad, vertically continuous downdraft at the RMW was also observed on the next pass out from the eye in the right-rear quadrant (Figs. 7a,b,d). This pass was along a radial about 60° counterclockwise (downstream) from the previous pass. Note the extreme width (approximately 10 km) of the downdraft, the dip in the flight level (Fig. 7a), and the positive temperature anomaly (Fig. 7e) that occurred during the traverse of the downdraft. This downdraft zone extended from the surface to 10 km. At flight level, the highest precipitation water content (Fig. 7c) was rather low in this downdraft; the 2D-P LWC was only 3 g m^{-3} in rain.

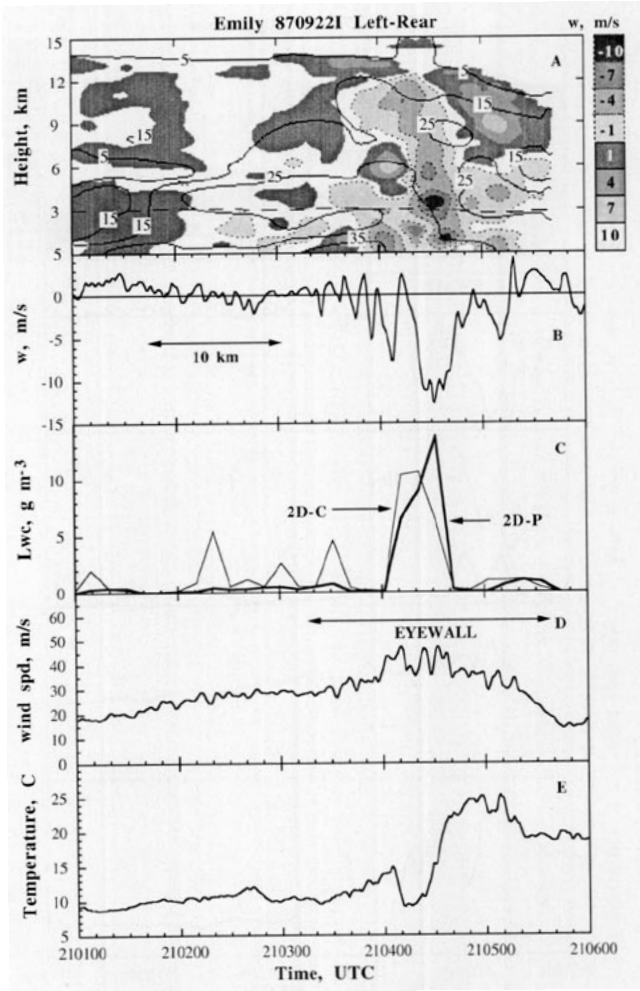

FIG. 6. As in Fig. 4 but for Doppler pass 15 in the left-rear quadrant.

d. *Upper aircraft flight-level data*

The vertical velocity profiles obtained by H near 5 km were similar to those obtained at 3 km. This similarity became apparent when the data from the radial passes in a quadrant from both aircraft containing one or more of the strongest cores were averaged with respect to the radius of maximum wind. The individual passes from H that contained the strongest and widest cores from each quadrant are shown, as well as the mean of all the legs for that quadrant.

1) LEFT-REAR QUADRANT

The strongest downdraft encountered at the 5-km level occurred in the left-rear quadrant at 1746:46 (Fig. 8a). It was located inside the RMW (Fig. 8d) and contained moderate cloud LWC (Fig. 8c); similar downdrafts were observed in this quadrant on almost every pass. Cloud liquid water contents measured by the JW spanned both the updraft at 1747:00 and the downdraft. Large aggregated ice particles with a number concentration of about 25 L^{-1} were observed in the 2D particle image data (not shown) after 1748:30. We attribute the rise in JW LWC from 1749 to 1751 UTC to large aggregates striking the sensor, not to cloud droplets. This time, temperature maxima a few degrees Celsius warmer than average were observed in both the inner edge of the large downdraft and in the updraft from 1747:20 to 1747:30. Although the peak updraft was nearly as strong as those in the front half of the storm (Table 1), the updrafts were more variable in magnitude and position relative to the RMW. The water contents from the 2D probes for this pass represent the sum of the ice water content and the liquid water content. These data indicate that the strong downdraft contained a modest amount of precipitation. In this case, the highest measured 2D water contents in the eyewall vertical velocity cores occurred in the period between the

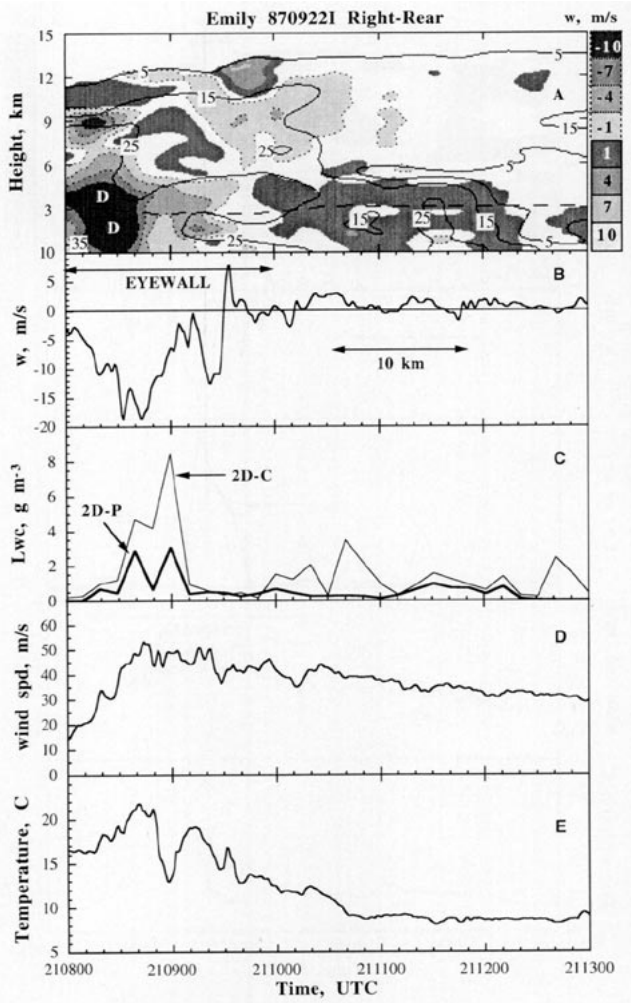

FIG. 7. As in Fig. 4 but for Doppler pass 16 in the right-rear quadrant.

downdraft and the inner updraft maximum from 1746:30 to 1747:30. The peaks of the total precipitation water contents at 5 km usually occurred either outside the RMW in regions that contain abundant large aggregated ice particles (e.g., Fig. 8b, 1750) or on the outer edge of the main eyewall updraft (1748:30–1749:10) where large graupel particles and raindrops were most abundant.

Vertical velocity and temperature deviations from the nine radial legs obtained in the left-rear quadrant over a 5-h interval by both aircraft were averaged relative to the RMW ($R = 0$) (Fig. 9). Although the relatively large variance in the averaged data (not shown) precludes statistical significance at the 95% level, the resemblance of the composite to individual profile data is striking. This composite clearly shows the strong downdrafts at $R = -4$ km and at $R = +2$ km, with an updraft in between at the RMW. The temperature deviations plotted with the composites were computed by subtracting the mean temperature at R greater than 10 km (i.e., outside the eyewall) from each leg from the measured temperature. The deviations computed in this way clearly show the warm-core nature of the hurricane. In general, the temperature deviations are greatest near the circulation center and decrease monotonically to near 0°C just beyond the RMW. Warming tends to be greater in storms with a smaller diameter eye than with a larger eye, all other parameters being equal (e.g., Hawkins and Imbembo 1976; LaSeur and Hawkins 1963). Our personal experience derived from over 200 radial penetrations of hurricane eyewalls has shown that maximum temperature deviations at the 5–6-km level are often in excess of 10°C in storms with eye diameters less than 40 km like Emily's. The small relative maximum in the temperature deviation profile at the position of the downdraft outside the RMW was contributed principally by data from the 3-km passes and is consistent with compressional warming within

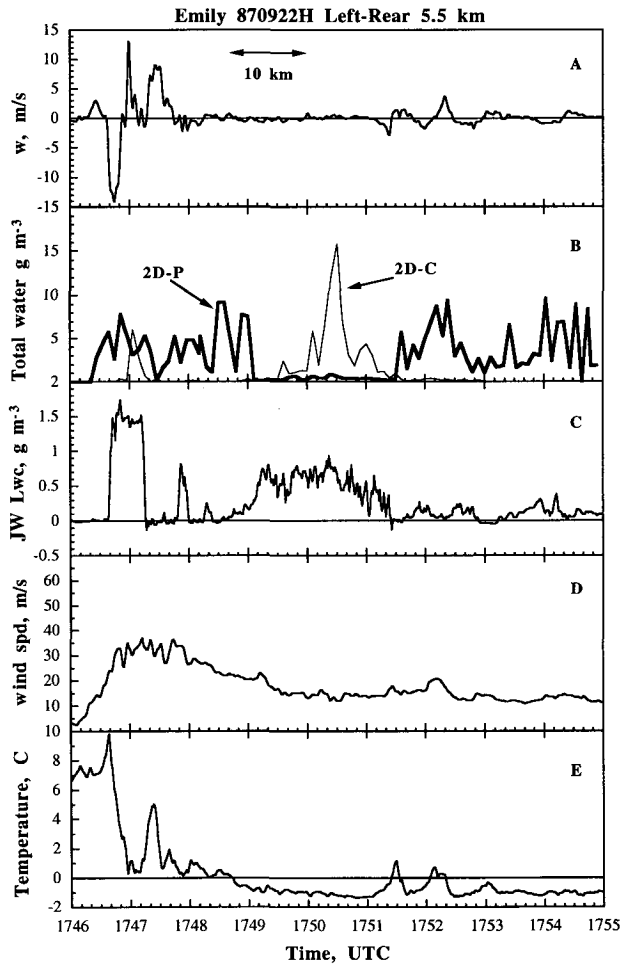

FIG. 8. Data from aircraft pass at 5.0 km in the left-rear quadrant. This pass features (a) the strongest mean downdraft and (b) a peak 2D-P precipitation water content of about 9 g m^{-3} in the updraft at 1747:00 UTC. Also shown are (c) cloud liquid water content (JW), (d) wind speed, and (e) temperature.

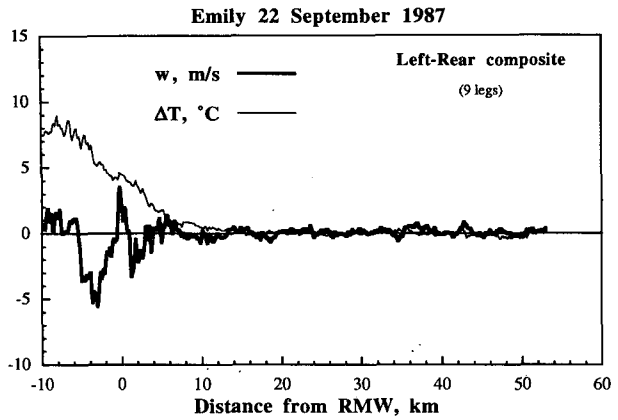

FIG. 9. Composite vertical velocity (thick line) and temperature deviation (thin line) profiles for the left-rear quadrant at flight level. All radial passes that contained one or more cores within the upper 10% of the population are included. Data are composited with respect to the RMW.

the downdrafts at that level. However, this relative maximum in temperature was not observed at 5 km in the downdraft cores inside the RMW.

2) THE RIGHT-REAR QUADRANT

The radial leg at 5 km in the right-rear quadrant from 1807:00 to 1814:00 (Fig. 10) shows a broad downdraft similar to that indicated by the Doppler data 3 h later plotted in Fig. 7. Although these data were obtained near the (stratiform area) melting level (Fig. 10e), both passes indicate a wide downdraft at the RMW (Figs. 10a,d). Very little precipitation is indicated in the downdraft at 1812:30. Weak updrafts marked by peaks in the JW LWC flanked this downdraft (Fig. 10c); the stronger of these updrafts was on the inside edge of the eyewall. The peak in the 2D water contents was encountered several kilometers radially outward from the peak downdraft (Fig. 10b). Again, we believe that the high JW water contents and the 2D-C water contents from 1809:30 to 1811:50 were caused by large melting aggregates that impact on the JW sensor and (in the case of the 2D probe data) are assigned an anomalously large bulk ice density. The temperature rise as the aircraft penetrated into the eye was almost 10°C, a large, but not unheard of value (e.g., Hawkins and Imbembo 1976).

Vertical velocity and temperature data were also averaged relative to the RMW for radial legs in the right-rear quadrant. In the composite, the strongest updraft (Fig. 11) was unusual because it occurred 6 km inside the RMW. The numerous wide downdrafts encountered in this quadrant are not so prominent in the composite because they were not at preferred distances from the RMW. No unusual temperature anomalies were revealed in this composite.

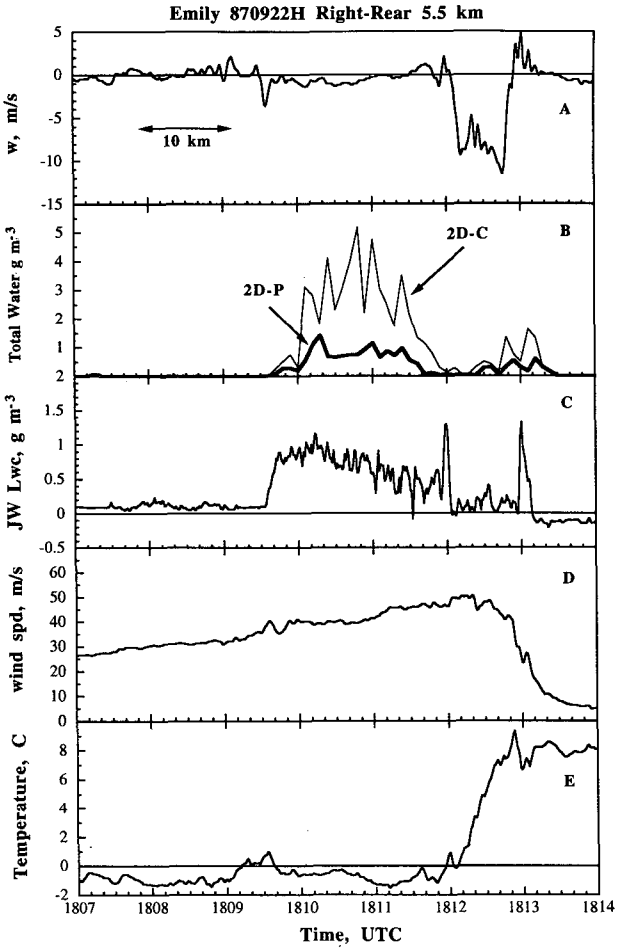

FIG. 10. As in Fig. 8 but for the right-rear quadrant.

3) LEFT-FRONT QUADRANT

In the left-front quadrant, H penetrated the eyewall through a very strong up–down–up draft sequence,

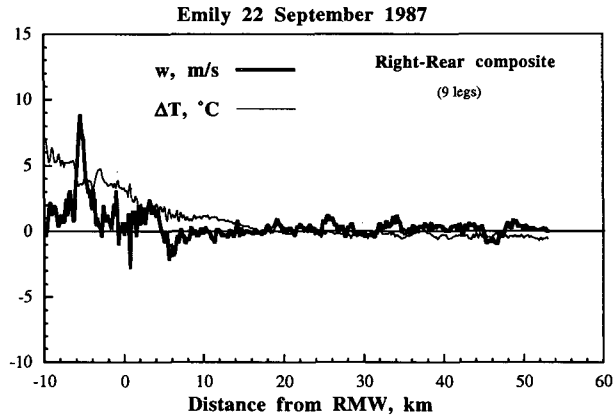

FIG. 11. As in Fig. 9 but for the right-rear quadrant.

with the main updraft inside the RMW at 2105 (Figs. 12a,d). The relative maximum in the 2D-C water content in the downdraft at 2105:45 (Fig. 12b) is due to many tiny ice particles having a peak 2D-C number concentration of 329 L^{-1}. High 2D-C number concentrations of small ice particles in the downdraft is common in hurricanes above the melting level (Black and Hallett 1986). Cloud liquid water contents as measured by the JW device reached a plateau in the updraft (Fig. 12c); however, the JW wire broke at 2105:27, and hence, no more data were collected. The strong downdraft at the RMW at 5.5 km (Fig. 12a) flanked by strong updrafts confirmed the Doppler analysis given in Fig. 5. No unusual temperature anomalies were observed during this pass.

The composite showed that powerful updrafts near the RMW flanked by strong downdrafts (Fig. 13) was a persistent feature of this quadrant for several hours. Almost every pass showed a similar profile, and the relative positions of the cores with respect to the RMW were maintained for hours.

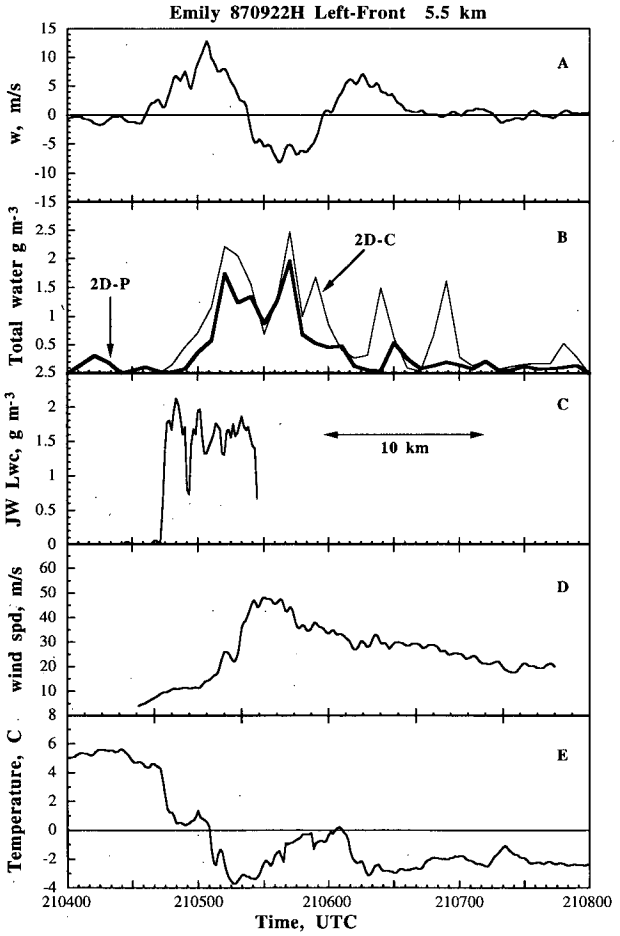

FIG. 12. As in Fig. 8 but at 5.5 km in the left-front quadrant. The JW liquid water sensor failed at 2105:28 UTC.

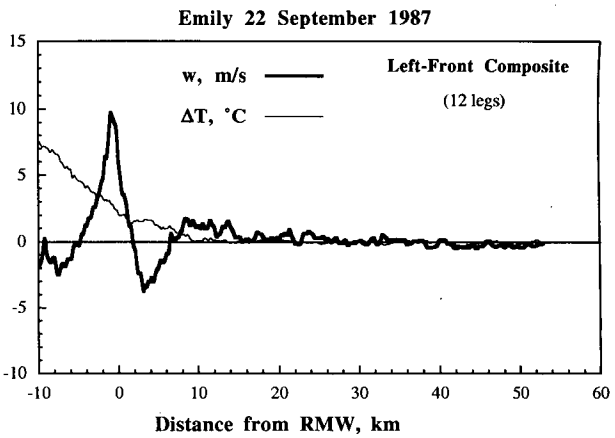

FIG. 13. As in Fig. 9 but for the left-front quadrant.

4) RIGHT-FRONT QUADRANT

The updrafts in this quadrant were observed at all flight levels. The Doppler data (e.g., Fig. 2) show that the updraft region was vertically contiguous from the surface to about 12 km, and the downdraft zone was strongest in the upper reaches of the eyewall, well above the flight levels. At the H flight levels, a broad, strong updraft at the RMW flanked by weak downdrafts (Figs. 14a,d) was typical of the right-front quadrant. These updrafts contained moderate precipitation water contents (Fig. 14b) and about 2 g m^{-3} of (supercooled) cloud liquid water (Fig. 14c). Relatively cool temperatures (Fig. 14e) were observed in the large updrafts, atypical of what is generally seen in buoyant convection, although some of this apparent cooling may be an anomaly caused by the impact of supercooled water on the temperature sensor.

The right-front composite (Fig. 15) exhibited the strongest and most persistent updraft of all. There are unusually high positive temperature anomalies at 3 km in the downdrafts beyond the RMW; this suggests that compressional warming occurred in these downdrafts at that altitude. The similarity between the composite for this quadrant (Fig. 15) and the flight-level data (Fig. 14) lend credence to the representativeness of the compositing procedure.

4. Summary and discussion

Updrafts and downdrafts on the order of 10–20 m s^{-1} were documented both by aircraft sensors and by vertically pointing Doppler radar. The mean updrafts and downdrafts were approximately twice as strong as those measured in other hurricanes. The mean width of the updrafts was approximately identical to the mean width of the downdrafts. The strongest updrafts and downdrafts were found in the front and rear quadrants of the storm, respectively. Many updrafts and downdrafts extended through a deep layer; some up-

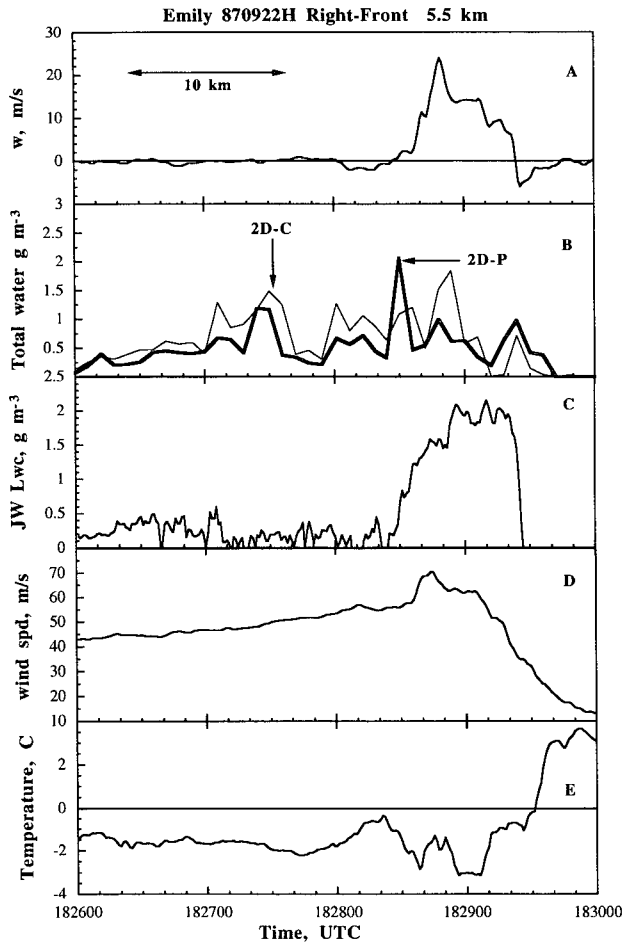

FIG. 14. Flight-level data from 5.5 km in the right-front quadrant. The strongest updraft peaked at 1828:45 UTC in the right-front quadrant.

drafts and downdrafts extended throughout the depth of the troposphere.

The conditions that caused the extreme vertical velocities in Emily must be relatively rare in hurricanes, because few other such cases have been observed in over 20 years of hurricane research. Strong updrafts are easier to explain using thermodynamic arguments than strong downdrafts. Except for the case of flow over a barrier, strong updrafts are always sustained by the conversion of thermodynamic potential energy in the form of latent heat of condensation and/or fusion to kinetic energy in convective clouds. Hurricanes are no exception to this rule. In the hurricane eyewall, rising parcels [which approximately conserve angular momentum (Jorgensen 1984b)] follow paths that slope radially outward and upstream. Thus, the updrafts are unloaded as precipitation falls out. In hurricanes, this process is generally so effective that total cloud and precipitation water contents near the melting level are much smaller than their adiabatic value (Black and Hallett 1986).

From parcel theory, the maximum vertical velocity w_{max} obtainable from the convective available potential energy (CAPE) is given by the relation

$$w_{max} = (2\ \mathrm{CAPE})^{1/2}. \quad (3)$$

This relation neglects water loading, entrainment, and nonhydrostatic vertical pressure gradient forces.

Air flowing into the hurricane eyewall and into rainbands is strongly modified by evaporation, both from the sea surface (Powell 1990) and from precipitation. Furthermore, a rising parcel that starts in the boundary layer can circle the eye (Marks and Houze 1987; Houze et al. 1992) before it reaches its maximum altitude. Computations of CAPE for the hurricane eyewall are therefore likely to be inaccurate because there are few soundings made closer than about 100 km from the eyewall, aircraft usually sample only a few levels, and the computations neglect precipitation loading. Even when an aircraft sounding is made, the sounding is seldom made near the eyewall because the heavy precipitation and strong horizontal winds make such maneuvers very hazardous. Dropsondes are also hampered and seldom work in precipitation. Furthermore, since hurricanes maintain large radial gradients of temperature, humidity, and horizontal wind speed across the eyewall, it is difficult to determine the appropriate "environmental" sounding for eyewall updrafts. Nevertheless, the existence of cumulus convection in the hurricane eyewall requires that its updraft air be buoyant. In the case of the strong updrafts in Emily, the rising air is necessarily more buoyant than usual.

Strong downdrafts in hurricane eyewalls are much more difficult to explain because a variety of effects contributes to them, and none is usually sufficient by itself to explain unusually vigorous downdrafts. These effects include evaporative cooling, precipitation drag, and melting of ice particles. Strongly convergent flow aloft and compensating motions in response to convective updrafts can also produce downdrafts. Furthermore, downdrafts in different quadrants of the eyewall

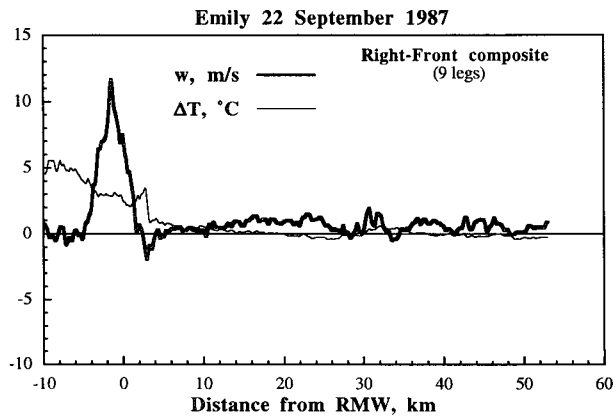

FIG. 15. As in Fig. 9 but for the right-front quadrant.

may have different combinations of mechanisms supporting them.

Downdrafts generated by evaporative and melting cooling and precipitation loading were studied in a recent paper by Srivastava (1987). Srivastava assumed that downdrafts caused by these processes were initiated at the melting level, and that the air below the melting level was dry. He found that if no ice particles were present and the lapse rate was nearly moist adiabatic (less than 6 K km^{-1}), the precipitation water mixing ratio had to be unusually large (LWC greater than approximately 14 g kg^{-1}) to generate 18 m s^{-1} downdrafts. With ice included, Srivastava found that for a lapse rate of 5 K km^{-1} (approximately the moist-adiabatic lapse rate at 5 km in the eyewall), an ice particle precipitation mixing ratio of approximately 10 g kg^{-1} is required at the melting level to produce an 18.6 m s^{-1} downdraft 2.0 km below that level.

In Emily at 5–6 km, the highest concentrations of precipitation-sized particles were almost always found on the outside edge of the eyewall well away from the locations of the strongest downdrafts. An examination of the strongest 10% downdraft data in Table 2 shows that the peak 2D-P water contents observed by H never exceeded 5.0 g kg^{-1} in the 14 strong downdrafts encountered near 5 km. Only 1 of those 14 downdrafts contained a peak 2D-C water content greater than 5 g kg^{-1}, and only 4 contained water contents in excess of 3 g kg^{-1}. The only downdrafts that contained at least 10 g kg^{-1} precipitation were observed at the 3.0-km level, where the temperature was approximately +10°C, well below the melting level. Therefore, thermodynamic processes alone are insufficient to account for the magnitudes of the downdrafts encountered in this storm, particularly those observed at 5 km and higher.

Moist symmetric instability (Emanuel 1986b) is a possible mechanism by which strong updrafts and downdrafts can be created in a saturated environment that is stable with respect to both vertical and horizontal perturbations (i.e., an environment that is both statically and inertially stable). We now investigate the possibility that moist symmetric instability may have occurred in Hurricane Emily, and that the intensity of the observed downdrafts and updrafts is consistent with theory. Kurihara (1975) demonstrated that the necessary condition for symmetric instability can be met in the upper levels of a simulated hurricane. Willoughby et al. (1982) and Willoughby et al. (1984) have suggested that symmetric instability at *upper levels* in hurricanes may play a role in triggering convective rings below. In this study we consider the possibility that moist symmetric instability may have occurred at *mid-levels* in the eyewall of a hurricane.

The frictionless equations of motion for a circularly symmetric vortex in a saturated atmosphere are as follows:

$$\frac{Du}{Dt} = \frac{v^2}{r} + fv - \frac{1}{\rho}\frac{\partial p}{\partial r} \tag{4}$$

$$\frac{Dv}{Dt} = -\frac{uv}{r} - fu \tag{5}$$

$$\frac{Dw}{Dt} = g\frac{(\theta_e' - \theta_e)}{\theta_e}, \tag{6}$$

where u, v, and w are the radial, azimuthal, and vertical velocities, r is the radial distance from the center of the vortex, p and ρ are the pressure and density, f is the Coriolis parameter, g is the acceleration of gravity, and θ_e' and θ_e are the equivalent potential temperatures of a ring of air at radius r and of the ring's environment, respectively. It has been assumed, as it is in the parcel theory of convection, that the pressure of a ring (a parcel at a given radius) displaced from its original position is the same as that of the environment into which it has been displaced.

Although hurricanes are not exactly circularly symmetric, we will neglect azimuthal variations in pressure in comparison to radial pressure variations near the eyewall. Asymmetries in the eyewall structure arise because of barotropic instability, vertical shear, friction from storm motion (Shapiro 1983), and varying horizontal wind in the environment along a storm's track (Marks et al. 1992). An additional cause of asymmetric structure may be the increased boundary layer friction caused by the mountains on Hispanola. Mountainous islands such as Hispanola are known to cause northward deflections in a storm's track and decreases in storm intensity (Bender et al. 1987). Case and Gerrish (1988) noted such effects on the structure and intensity of Hurricane Emily.

The absolute angular momentum,

$$M = r\left(v + \frac{fr}{2}\right), \tag{7}$$

is the angular momentum due to both the rotation of the vortex and the rotation about the earth's axis. It follows from (5) and (7) that

$$\frac{DM}{Dt} = 0, \tag{8}$$

that is, that M is conserved in a frictionless atmosphere. It also follows from (7) that the radial equation of motion (4) may be expressed as

$$\frac{Du}{Dt} = \frac{(M - M_{gr})(M + M_{gr})}{r^3}, \tag{9}$$

where M_{gr} is the M of a nonmoving vortex in gradient wind balance.

Suppose that the θ_e surfaces in the eyewall of a hurricane are vertically oriented as they are, to a rough approximation, in the observational analyses of Hawkins and Imbembo (1976) and Jorgensen (1984b), and

in the numerical simulations of Rotunno and Emanuel (1987). The absolute angular momentum surfaces tend also to be vertically oriented in the eyewall (in the numerical simulations, θ_e and M surfaces are parallel to each other) and flare out at high levels and at farther distances from the center in response to the hurricane's secondary circulation. Figure 16 shows schematically the idealized distributions of M and θ_e surfaces in the eyewall of a hurricane (between the boundary layer and the tropopause) in which the θ_e and M surfaces have been rearranged to produce a moist symmetrically unstable configuration. Consider what restoring forces act upon a ring of air near location A in Fig. 16 using (9) and (6): If the ring is displaced downward (perhaps as a result of water loading) to B, and does not mix with its environment, then it experiences no vertical restoring force, because it lies along its original θ_e surface. However, it moves into a region in which M_{gr} is greater than the M of the ring, which is conserved; hence, according to (9) it is accelerated radially inward to C. As it does, it moves into a region in which its θ_e is less than that of its environment, and hence it also accelerates downward. The net result is a slantwise (radially inward and downward) trajectory; negatively buoyant downdrafts are possible because the ring is accelerated radially inward to a warmer environment.

Since the curl of the restoring force acting on the ring [see Eqs. (9) and (6)] is zero, an integral of the restoring force is path independent. The work done on the ring by the environment can therefore be computed by integrating the restoring force from the initial location of the ring (z), down to any level (z') along an M_{gr} surface. This work is called the slantwise convective available potential energy (SCAPE), where

$$\text{SCAPE}(z') = \int_z^{z'} g\left(\frac{\theta_e' - \theta_e}{\theta_e}\right) dz M_{gr}. \quad (10)$$

The vertical velocity of the downdraft at height z', if the ring initially were at rest, is given by

$$w(z') = -(2\ \text{SCAPE})^{1/2}. \quad (11)$$

This relation, like (3), neglects water loading, entrainment, and nonhydrostatic vertical pressure gradient forces. Our analysis is similar to that of the parcel/tube analysis of Emanuel (1986b) but is modified for application to a circularly symmetric vortex.

To see if downdrafts in Hurricane Emily as great as 15–20 m s^{-1} (cf. Tables 1 and 2) could have been realized by moist symmetric instability, we evaluated (10) and (11) in the following manner. Vertical cross sections of M averaged from all the legs in each quadrant of the hurricane (Figs. 17a–d) were analyzed from the airborne Doppler radar data using the technique employed by Marks et al. (1992). The 3D wind field was derived using the "pseudo"– dual-Doppler analysis technique. A coordinate system relative to the storm circulation center at all altitudes was defined, and the storm-relative mean azimuthal wind component was determined. There are some regions aloft that appear to be inertially unstable ($\partial M/\partial r < 0$). However, the M computations aloft are less reliable because the radar reflectivity is relatively weak.

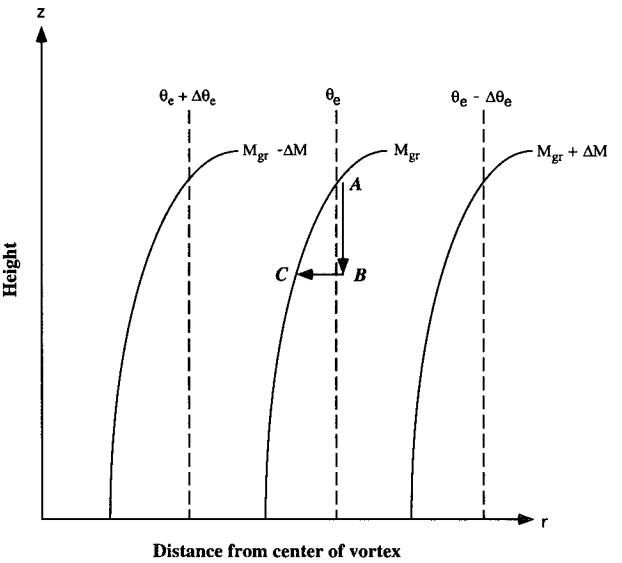

FIG. 16. Idealized vertical cross section of absolute angular momentum M (solid contours) and equivalent potential temperature θ_e (dashed contours) in the eyewall of a hurricane, above the boundary layer and below the tropopause. Here M_{gr} denotes the M of a vortex in gradient wind balance.

Using the average M cross section and θ_e radial profile at 5 km for the right-rear quadrant (Fig. 17b), we integrated from r = 15 km, z = 8, in the eyewall in a region of relatively high radar reflectivity, along the M_{gr} = 5.5 × 10^{-5} m^2 s^{-1} contour, down to r = 13 km, z = 5 km, at the higher flight level (Fig. 10) where strong downdrafts had been measured; it was assumed for simplicity that $\partial\theta_e/\partial z = 0$. In the region of the integration, the horizontal temperature gradient was relatively strong at 5 km (Fig. 17b). The SCAPE for the aforementioned vertical and horizontal excursions is approximately 125 J kg^{-1}, which is enough to produce a downdraft as strong as 16 m s^{-1}. If a downdraft had been initiated from an even higher level, or if an updraft had been initiated from below flight level, the SCAPE would have been even larger, and consequently the vertical velocities could have been even stronger. It thus appears as if moist symmetric instability could have been responsible for the unusually strong vertical velocities observed.

What was unusual about the structure of Hurricane Emily that could have permitted moist symmetric instability? Are the necessary conditions for moist symmetric instability not realized in other hurricanes in which weaker vertical velocities have been observed? If the θ_e surfaces are steeply oriented in the eyewall, then the SCAPE is to a rough approximation a function

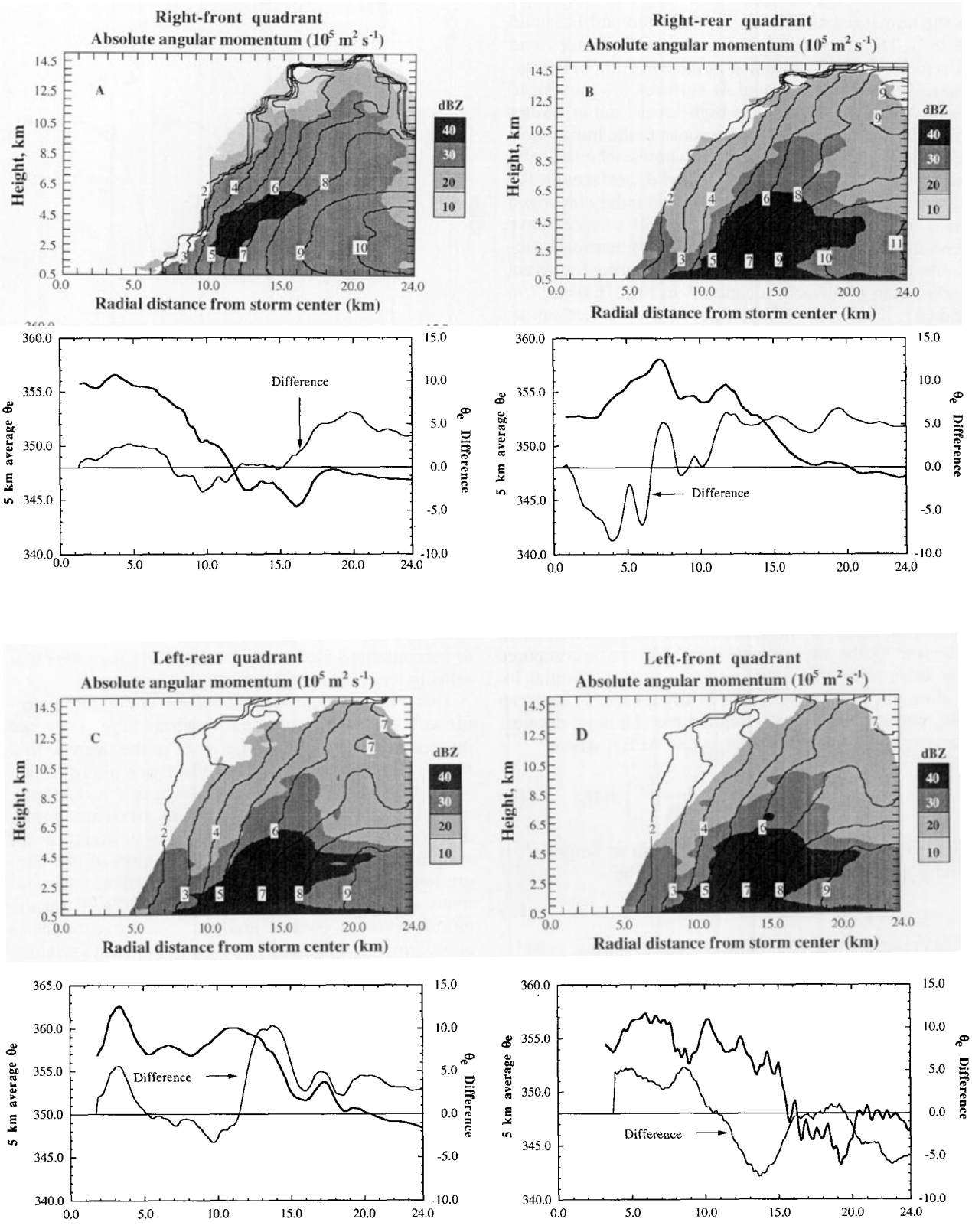

FIG. 17. Vertical cross sections of M (10^5 m^2 s^{-1}) in Hurricane Emily in the following quadrants: (a) right front, (b) right rear, (c) left rear, and (d) left front. Composites are valid for 1538–1744 UTC 22 September 1987. Average radar reflectivity in the range 10–40 dBZ is superimposed on the M plot. The mean quadrant θ_e from the H aircraft, and the θ_e difference H − I (i.e., the difference between θ_e at the higher level and θ_e at the lower level) are plotted. These data have been smoothed with a nine-point Gaussian filter for clarity.

of the radially outward slope of the M surfaces. The hurricane is symmetrically unstable with respect to saturated slantwise displacements if the M surfaces lean outward more than the θ_e surfaces, and the amount of instability is proportional to how sharply the M surfaces lean outward. We therefore also considered for comparison the analyses of M surfaces in other hurricanes, which had weaker flight-level updrafts and downdrafts.

The slope of the M surfaces in the eyewall of Hurricane Emily at midlevels (i.e., 7 km MSL) are compared in Table 3 to the slope of the M surfaces shown in Jorgensen (1984b, Fig. 12) for Hurricane Allen (1980), in Hawkins and Imbembo (1976, Fig. 21) for Hurricane Inez (1966), and in Rotunno and Emanuel (1987, Fig. 11) for an axisymmetric numerical simulation. Table 3 also indicates the slope of M surfaces in analyses we computed of vertical cross sections averaged by quadrant in Hurricanes Norbert (1984), Gloria (1984), Gilbert (1988), Hugo (1989), and Jimena (1991), all of which were moderately strong-to-intense hurricanes. The slope of the M surfaces at midlevels in Emily are not unusual; the slope of the M surfaces in Emily's eyewall at midlevels is greater than that in Hugo, Allen, and the Rotunno–Emanuel simulations, but less than that in Gilbert. Emily's M surfaces were not flared out more than those in other hurricanes. If SCAPE is a function of the slope of the M surfaces, then there is no indication that SCAPE was higher in Emily than in other hurricanes. There also does not appear to be a relationship between the deepening (or filling) rate and the slope of M surfaces.

Our analyses therefore suggest that although moist symmetric instability can account for the strong updrafts and downdrafts observed in Emily, it is not apparent why this process would have occurred with more vigor in Emily than in other hurricanes. It has been found that cumulus convection in the Tropics tends to be nearly in statistical equilibrium with its large-scale forcing (e.g., Arakawa and Schubert 1974). Betts (1982) and Xu and Emanuel (1989) presented evidence that the tropical atmosphere is approximately neutral to parcels lifted *reversibly* (i.e., if the condensed water remains with the air parcel) from the *top* of the subcloud layer. Since deep convection in the hurricane eyewall is always accompanied by heavy precipitation, this condition is not satisfied there. Xu and Emanuel (1989) suggested that an increase in mixed layer equivalent potential temperature is necessary for the generation of kinetic energy, and that this could occur as a result of an air–sea interaction instability that involves a coupling between surface fluxes of sensible heat and water vapor, and the surface winds (Emanuel 1986a; Rotunno and Emanuel 1987).

There has been some evidence that the lightning flash rate in the Tropics increases with increasing CAPE (Williams et al. 1992), and that rapid deepening in hurricanes may be related to vigorous convection, as evidenced by lightning activity (Black et al. 1986a). The H aircraft was in fact struck by lightning at least twice in Emily's eyewall. In rapidly deepening tropical cyclones an enhanced surface flux of equivalent potential temperature can produce a moist symmetrically unstable configuration of M and θ_e surfaces by steepening the latter with respect to the former. Evaporative cooling along the inner edge of the top of the eyewall as dry air is entrained into it can decrease θ_e aloft, and also steepen the θ_e surfaces with respect to the M surfaces. Cooling due to melting can also have the same effect. We speculate that during Emily's rapidly deepening phase, the hurricane vortex was knocked out of dynam-

TABLE 3. Comparative characteristics of eight hurricanes and a simulated hurricane. The M surface slopes are computed from Doppler analyses in all cases except Inez and the simulated hurricane; LF—left-front quadrant, RF—right-front quadrant, RR—right-rear quadrant, and LR—left-rear quadrant.

Case	Outward slope of M surfaces at 7 km in the eyewall				Surface pressure at center (mb)	24-h Δp (mb)	Category (Saffir–Simpson scale)
	LF	RF	RR	LR			
Inez (1966)		←1.0[a]→			927	−35	5
Allen (1980) 5 August		←0.5[a]→			935	+21[b]	4
Allen (1980) 8 August		←1.0[a]→			920	−122[c]	4
Norbert (1984)	1.4	1.1	1.6	1.5	950	+9	3
Gloria (1985)	1.5	2.0	2.0	1.4	950	−37	4
Emily (1987)	1.4	1.1	1.3	1.6	958	−60	3
Gilbert (1988)	4.0	2.0	3.5	5.6	889	−63	5
Hugo (1989)	0.8	0.8	0.7	0.7	943	+16	4
Jimena (1991)	0.9	1.0	1.1	1.2	947	n/a	4
Simulation 80 h		←0.7[d]→					
Simulation 120 h		←0.8[d]→					

[a] Extrapolated above 6.5 km; mean for all quadrants.
[b] Based on 5-h 45-min tendency.
[c] Based on 2-h 43-min tendency.
[d] (Rotunno and Emanuel 1987) axisymmetric model mean value.

ical balance, and that slantwise adjustments occurred that brought the vortex back into dynamical balance. It is also possible that asymmetries in the vortex (the tilt of the M surfaces varied from quadrant to quadrant; see Table 3) led to the production of M surfaces that tilted outward more than the θ_e surfaces. In any event, the M and θ_e surfaces associated with the secondary circulation became congruent—that is, neutral with respect to moist symmetric instability—after "vigorous mixing," as in Rotunno and Emanuel's (1987) simulation.

The quadrant statistics showed that the bulk of the upward motions occurred in the front quadrants, whereas the rear quadrants contained mostly downdrafts. This pattern is common in hurricanes, and it is attributed to the effect of storm motion on the wind field (Willoughby 1988). We found in many instances that strong downdrafts were located just inside and just outside the eyewall updraft at the RMW (e.g., Fig. 13). This pattern of downdrafts and updrafts is suggestive of a standing-wave-like phenomenon. We speculate that the rapid deepening rate of the hurricane was associated with dynamical imbalances that may have been responsible for the triggering of high-amplitude gravity waves.

There are other mechanisms by which intense updrafts or downdrafts could be generated. For example, Ekman pumping could be responsible for some of the rising motion we documented. However, Ekman pumping should be related to storm intensity, not to the intensification rate of the storm. Rotunno and Klemp (1982) and Brandes et al. (1988) showed theoretically and observationally, respectively, how a strong buoyant updraft acting in an environment of strong vertical shear can induce vertical pressure perturbation gradient forces capable of inducing significant vertical motion. Although updrafts are strong in the hurricane eyewall, vertical shear is weak (e.g., Marks et al. 1992). If there are small-scale vortices within the eyewall, they may be intense enough to induce strong vertical motions. However, they may be too narrow to explain the width of the observed updrafts and downdrafts. It is also possible that vertical vorticity associated with horizontal shear just inside and outside the RMW is tilted into the horizontal vorticity associated with horizontal gradients of vertical velocity. Unfortunately, Doppler radar analysis of the horizontal wind field was not possible on short enough timescales to test this hypothesis. We look forward, however, to future airborne datasets collected with both forward and aft-scanning Doppler radar beams on one aircraft and true dual-Doppler data, both of which can be analyzed on smaller timescales.

Acknowledgments. We thank the many people who contributed to this work. The flight crews of NOAA AOC endure many uncomfortable flight hours in order to study these storms, and the engineers are especially commended for keeping the equipment running in spite of severe turbulence. The constructive comments and criticisms of this work provided by Drs. Robert Burpee, John Gamache, Frank Marks, and Hugh Willoughby of HRD, and Fred Sanders, Lance Bosart, John Molinari, Rich Rotunno, and an anonymous reviewer greatly improved this paper. H. Bluestein was supported in part by NSF Grants ATM-9019821 and ATM-9302379.

REFERENCES

Arakawa, A., and W. H. Schubert, 1974: Interaction of a cumulus cloud ensemble with the large-scale environment, Part I. *J. Atmos. Sci.*, **31,** 674–701.

Axford, D. N., 1968: On the accuracy of wind measurements using an inertial platform in an aircraft, and an example of a measurement of the vertical mesostructure of the atmosphere. *J. Appl. Meteor.*, **7,** 645–666.

Bender, M. A., R. E. Tuleya, and Y. Kurihara, 1987: A numerical study of the effect of island terrain on tropical cyclones. *Mon. Wea. Rev.*, **115,** 130–155.

Betts, A. K., 1982: Saturation point analysis of moist convective overturning. *J. Atmos. Sci.*, **39,** 1484–1505.

Black, M. L., 1993: Comparisons of tropical cyclone intensity with eyewall vertical velocities. *Proc. 20th Conf. on Hurricanes and Tropical Meteorology,* San Antonio, TX, Amer. Meteor. Soc., 520–523.

Black, P. G., R. A. Black, J. Hallett, and W. A. Lyons, 1986a: Electrical activity of the hurricane. Preprints, *23d Conf. on Radar Meteorology,* Snowmass, CO, Amer. Meteor. Soc., J277–J280.

——, F. D. Marks Jr., and R. A. Black, 1986b: Supercell structure in tropical cyclones. *Proc. 23d Conf. on Radar Meteorology,* Snowmass, CO, Amer. Meteor. Soc., 255–259.

Black, R. A., 1990: Radar reflectivity–ice water content relationships for use above the melting level in hurricanes. *J. Appl. Meteor.*, **29,** 955–961.

——, and J. Hallett, 1986: Observations of the distribution of ice in hurricanes. *J. Atmos. Sci.*, **43,** 802–822.

Bluestein, H. B., and G. Woodall, 1990: Doppler-radar analysis of a low-precipitation severe storm. *Mon. Wea. Rev.*, **118,** 1640–1664.

Brandes, E., R. Davies-Jones, and B. Johnson, 1988: Streamwise vorticity effects on supercell morphology and persistence. *J. Atmos. Sci.*, **45,** 947–963.

Case, R. A., and H. P. Gerrish, 1988: Annual summary Atlantic hurricane season of 1987. *Mon. Wea. Rev.*, **116,** 939–949.

Ebert, E. E., and G. J. Holland, 1992: Observations of record cold cloud-top temperatures in Tropical Cyclone Hilda (1990). *Mon. Wea. Rev.*, **120,** 2240–2251.

Emanuel, K. A., 1986a: An air–sea interaction theory for tropical cyclones. Part I: Steady-state maintenance. *J. Atmos. Sci.*, **43,** 585–604.

——, 1986b: Lagrangian parcel dynamics of moist symmetric instability. *J. Atmos. Sci.*, **40,** 2368–2376.

Hawkins, H. F., and S. M. Imbembo, 1976: The structure of a small, intense hurricane, Inez 1966. *Mon. Wea. Rev.*, **104,** 418–442.

Holliday, C. R., and A. H. Thompson, 1979: Climatological characteristics of rapidly intensifying typhoons. *Mon. Wea. Rev.*, **107,** 1022–1034.

Houze, R. A., Jr., F. D. Marks Jr., and R. A. Black, 1992: Dual-aircraft investigation of the inner core of Hurricane Norbert. Part II: Mesoscale distribution of ice particles. *J. Atmos. Sci.*, **49,** 943–962.

Jorgensen, D. P., 1984a: Mesoscale and convective-scale characteristics of mature hurricanes. Part I: General observations by research aircraft. *J. Atmos. Sci.*, **41,** 1268–1285.

——, 1984b: Mesoscale and convective-scale characteristics of mature hurricanes. Part II: Inner core structure of Hurricane Allen (1980). *J. Atmos. Sci.*, **41,** 1287–1311.

——, and M. A. LeMone, 1989: Vertical velocity characteristics of oceanic convection. *J. Atmos. Sci.*, **46,** 621–640.

——, E. J. Zipser, and M. A. LeMone, 1985: Vertical motions in intense hurricanes. *J. Atmos. Sci.*, **42,** 839–856.

Knollenberg, R. G., 1972: Comparative liquid water content measurements of conventional instruments with an optical array spectrometer. *J. Appl. Meteor.*, **11,** 501–508.

Kurihara, Y., 1975: Budget analysis of a tropical cyclone simulated in an axisymmetric numerical model. *J. Atmos. Sci.*, **32,** 25–59.

LaSeur, N. E., and H. F. Hawkins, 1963: An analysis of Hurricane Cleo (1958) based on data from research reconnaisance aircraft. *Mon. Wea. Rev.*, **91,** 694–709.

LeMone, M. A., and E. J. Zipser, 1980: Cumulonimbus vertical velocity events in GATE. Part I: Diameter, intensity, and mass flux. *J. Atmos. Sci.*, **37,** 2444–2457.

Marks, F. D., Jr., and R. A. Houze Jr., 1987: Inner core structure of Hurricane Alicia from airborne Doppler radar observations. *J. Atmos. Sci.*, **44,** 1296–1317.

——, ——, and J. F. Gamache, 1992: Dual-aircraft investigation of the inner core of Hurricane Norbert. Part I: Kinematic structure. *J. Atmos. Sci.*, **49,** 919–942.

Powell, M. D., 1990: Boundary layer structure and dynamics in outer hurricane rainbands. Part II: Downdraft modification and mixed layer recovery. *Mon. Wea. Rev.*, **118,** 918–938.

Rotunno, R., and J. Klemp, 1982: The influence of shear-induced pressure gradient on thunderstorm motion. *Mon. Wea. Rev.*, **110,** 136–151.

——, and K. A. Emanuel, 1987: An air–sea interaction theory for tropical cyclones. Part II: Evolutionary study using a nonhydrostatic axisymmetric numerical model. *J. Atmos. Sci.*, **44,** 542–561.

Shapiro, L. J., 1983: The asymmetric boundary layer flow under a translating hurricane. *J. Atmos. Sci.*, **40,** 1984–1998.

Srivastava, R. C., 1987: A model of intense downdrafts driven by the melting and evaporation of precipitation. *J. Atmos. Sci.*, **44,** 1752–1773.

Williams, E. R., S. A. Rutledge, S. G. Geotis, N. Renno, E. Rasmussen, and T. Rickenbach, 1992: A radar and electrical study of tropical "hot towers." *J. Atmos. Sci.*, **49,** 1386–1395.

Willoughby, H. E., 1988: Linear motion of a shallow-water barotropic vortex. *J. Atmos. Sci.*, **45,** 1906–1928.

——, J. A. Clos, and M. G. Shoreibah, 1982: Concentric eyewalls, secondary wind maxima, and the evolution of the hurricane vortex. *J. Atmos. Sci.*, **39,** 395–411.

——, H.-L. Jin, S. J. Lord, and J. M. Piotrowicz, 1984: Hurricane structure and evolution as simulated by an axisymmetric, nonhydrostatic numerical model. *J. Atmos. Sci.*, **41,** 1169–1186.

Xu, K.-M., and K. Emanuel, 1989: Is the tropical atmosphere conditionally unstable? *Mon. Wea. Rev.*, **117,** 1471–1479.